

From discrete to continuum models of three-dimensional deformations in epithelial sheets

N. Murisic, V. Hakim, I. Kevrekidis, S. Y. Shvartsman, B. Audoly

▶ **To cite this version:**

N. Murisic, V. Hakim, I. Kevrekidis, S. Y. Shvartsman, B. Audoly. From discrete to continuum models of three-dimensional deformations in epithelial sheets. Biophysical Journal, 2015, 109 (1), pp.154-163. 10.1016/j.bpj.2015.05.019 . hal-01175718

HAL Id: hal-01175718
https://hal.science/hal-01175718

Submitted on 15 Jul 2015

HAL is a multi-disciplinary open access archive for the deposit and dissemination of scientific research documents, whether they are published or not. The documents may come from teaching and research institutions in France or abroad, or from public or private research centers.

L'archive ouverte pluridisciplinaire **HAL**, est destinée au dépôt et à la diffusion de documents scientifiques de niveau recherche, publiés ou non, émanant des établissements d'enseignement et de recherche français ou étrangers, des laboratoires publics ou privés.

From discrete to continuum models of three-dimensional deformations in epithelial sheets

N. Murisic[1], V. Hakim[2], I. G. Kevrekidis[3], S. Y. Shvartsman[1] and B. Audoly[4]

[1]Lewis-Sigler Institute for Integrative Genomics, Princeton University, Princeton, New Jersey, 08544, USA
[2]CNRS & Laboratoire de Physique Statistique, Ecole Normale Supérieure, 24 rue Lhomond 75231 Paris Cedex 05, France
[3]Chemical and Biological Engineering, Princeton University, Princeton, New Jersey, 08544, USA
[4]Sorbonne Universités, UPMC Univ Paris 06, CNRS, UMR 7190 Institut Jean Le Rond d'Alembert, F-75005 Paris, France

July 12, 2015

Abstract

Epithelial tissue, in which cells adhere tightly to each other and to the underlying substrate, is one of the four major tissue types in adult organisms. In embryos, epithelial sheets serve as versatile substrates during the formation of developing organs. Some aspects of epithelial morphogenesis can be adequately described using vertex models, in which the two-dimensional arrangement of epithelial cells is approximated by a polygonal lattice with an energy that has contributions reflecting the properties of individual cells and their interactions. Previous studies with such models have largely focused on dynamics confined to two spatial dimensions and analyzed them numerically. We show how these models can be extended to account for three-dimensional deformations and studied analytically. Starting from the extended model, we derive a continuum plate description of cell sheets, in which the effective tissue properties, such as bending rigidity, are related explicitly to the parameters of the vertex model. To derive the continuum plate model, we duly take into account a microscopic shift between the two sublattices of the hexagonal network, which has been ignored in previous work. As an application of the continuum model, we analyze tissue buckling by a line tension applied along a circular contour, a simplified set-up relevant to several situations in the developmental context. The buckling thresholds predicted by the continuum description are in good agreement with the results of direct stability calculations based on the vertex model. Our results establish a direct connection between discrete and continuum descriptions of cell sheets and can be used to probe a wide range of morphogenetic processes in epithelial tissues.

Keywords: vertex model; elastic plates; buckling; Cauchy-Born rule; homogenization

1 Introduction

The emergence of epithelial tissues, in which polarized cells adhering to each other and to the extracellular matrix are arranged in continuous sheets, was one of the key steps in the evolution of multilcellular animals. In adult organisms, epithelia line the internal surfaces of organs, maintaining their integrity and mediating interactions between different compartments. During embryonic development, epithelia serve as the starting point in the morphogenesis of tissues and organs (1). Epithelial morphogenesis can be accompanied by changes in cell numbers, due to cell division and death. At the same time, early steps in a number of important and well-studied morphogenetic events, including early stages of gastrulation (2), happen at constant cell

numbers and do not involve changes in cell connectivity. This is the class of processes considered in this paper, in which we aim to develop a coarse-grained description of three-dimensional tissue deformations, starting from cell-level description of an epithelium.

Recent studies of epithelial morphogenesis (3–7) provide highly resolved kinematic descriptions that set the stage for the development and analysis of mathematical models that can explain and predict the observed cell and tissue deformations. Some of the simplest proposed mathematical descriptions are the so-called *vertex models*, see (3, 8–14), in which the degrees of freedom are the coordinates of the vertices of cells, modelled as planar polygons. The energy of such a model epithelium is evaluated from contributions of terms that account for properties of individual cells, like the preference for a target area value and their tendency to minimize perimeter length due to cortical tension. It also includes cell pairwise interactions, modelled as terms depending on the length of cell-cell edges, as in e.g. (3). Of course, tissue morphogenesis is quite varied and a number of phenomena such as cell motion, have been described by models different from vertex models, see (15) for a review. Vertex models have been used to explain the statistics of cell shapes and compartment boundaries in developing epithelia and provide a clear connection between experimental data and simple physical theories (3, 12, 16, 17). Here, we use the existing models as a starting point for describing out-of-plane deformations of epithelial sheets.

Our results can be summarized as follows. First, we show that a three-dimensional extension of vertex models requires some care in the definition of cell area, which is straightforward when cells are planar, but must be redefined when vertices can move in three dimensions. In order to properly describe three-dimensional deformations, we also introduce a cell-based description of bending stresses. Second, we use a homogenization approach to derive an effective continuum description of an epithelium, valid on length scales larger than a single cell. Motivated by a number of experimental studies, e.g. (17), we use the homogenized model to describe epithelial buckling induced by heterogeneities of cell properties. Linear stability analysis of the homogenized problem is in quantitative agreement with the results of direct bifurcation analyses of the extended vertex model that resolves individual cells, suggesting that our approach can describe a wide range of phenomena in developing epithelia.

2 Materials and methods

2.1 The non-planar vertex model

Originally developed to study foams (18), vertex-based geometrical models have been employed to describe cell sheets since the early work of Honda (8, 9). In this approach (3, 4, 11–13, 16), interfaces between cells are defined as straight segments and each cell assumes a polygonal shape. Cell dynamics is described in a simplified way in terms of the motion of the polygon vertices.

Based on these previous works, we introduce a vertex model to describe non-planar configurations of epithelial cell sheets. We consider a smooth surface endowed with a mesh, as described schematically in Figure 1. More precisely, the lattice is specified by the positions $\mathbf{x}_v$ of its vertices, where v is a vertex index. The length L_e of an edge labelled by e is $L_e = |\mathbf{x}_{v_2(e)} - \mathbf{x}_{v_1(e)}|$, where $v_1(e)$ and $v_2(e)$ denote the indices of the vertices at the endpoints of the edge e. The perimeter P_f of a face f is simply the sum of the lengths of its edges e, $P_f = \sum_{e\in f} L_e$.

Next, the energy of a non-planar configuration of cells is defined by

$$\mathcal{E}_{\mathrm{vm}} = \frac{1}{2}\sum_f (A_f - 1)^2 + G\sum_e L_e + \frac{H}{2}\sum_f {P_f}^2 + B\sum_{e'}\left(1 - \mathbf{N}_{f_1(e')}\cdot\mathbf{N}_{f_2(e')}\right). \tag{1}$$

The first and third term run over all faces f, the second term over all edges e, and the last term runs over *interior* edges e' *i.e.* edges belonging to *two* adjacent faces $f_1(e')$ and $f_2(e')$. The quantities G, H and B are elasticity parameters. The first term (area elasticity) penalizes any deviation from the natural area $A^0 = 1$. For simplicity, we work in a set of units such that both the target area A^0 and the corresponding modulus have the value 1. The second term captures the adhesion energy between cells, when $G < 0$. The coefficient G has units of energy per unit length, or force. The third term represents cortical tension

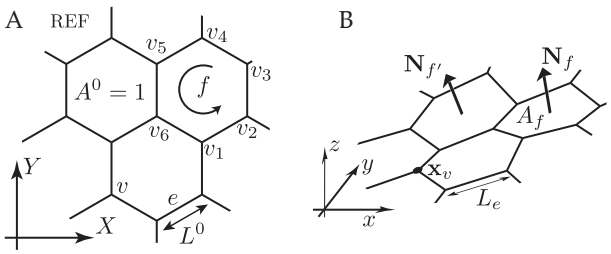


Figure 1: **The 3D vertex model**. A. Schematic drawing of the hexagonal vertex model, showing the vertices, edges and cell faces in reference configuration. B. Deformation of the reference regular hexagonal configuration into a non-planar configuration, and unit outward normal vectors.

(perimeter elasticity). The last term is a bending term to which we will return below. A simpler description is often used with $H = 0$ and $G > 0$, which then represents an effective line tension. In the following, we provide analytical results for the general case $G \neq 0, H \neq 0$ and focus on the case $H = 0$ in our simulations.

For planar configurations of the vertices, the bending term vanishes and the energy defined by Eq. (1) coincides with the classical, planar vertex model (3, 13). For non-planar configurations, the area A_f and the unit normal $\mathbf{N}_f$ to a face f appearing in equation (1) can be defined in different ways (19) which are all equivalent in the continuous limit. We use the following definitions, which differ slightly from those used in (17) and are more convenient. Let n be the number of vertices of the face f ($n = 6$ for a hexagonal mesh), and $(v_1(f), \ldots, v_n(f))$ be the list of vertices ordered in the counter-clockwise direction, as in figure 1. We first define the *vector* area $\mathbf{A}_f$ of the face f by

$$\mathbf{A}_f = \frac{1}{2}\left(\mathbf{x}_{v_1(f)} \times \mathbf{x}_{v_2(f)} + \mathbf{x}_{v_2(f)} \times \mathbf{x}_{v_3(f)} + \cdots + \mathbf{x}_{v_n(f)} \times \mathbf{x}_{v_1(f)}\right), \tag{2}$$

this quantity being invariant under rigid-body translations of the lattice. Next, we define the *scalar* area A_f and the unit normal $\mathbf{N}_f$ by

$$A_f = |\mathbf{A}_f|, \qquad \mathbf{N}_f = \frac{\mathbf{A}_f}{A_f}. \tag{3}$$

Observing that the flux of a constant vector field $\mathbf{u}$ through the face f is expressed as $\mathbf{A}_f \cdot \mathbf{u}$, we can interpret these definitions geometrically: $\mathbf{N}_f = \mathbf{u}$ is the unit vector producing the maximum flux across the face, and A_f is the maximal value of the flux.

Once the area of a face is defined, the energy of a non-planar configuration of vertices can be computed. The usual first three terms on the right-hand-side of Eq. (1) penalize bending deformations only weakly, see §3.1. They produce a bending modulus for the epithelial sheet that is entirely determined by the 2D biophysical parameters $(A^0 = 1, G, H)$ and that moreover depends on the somewhat arbitrary definition of the discrete area $\mathbf{A}_f$. Therefore, in order to produce a better defined model, adaptable to diverse biological contexts, we have added the last term in the r.h.s. of Eq. (1). It is a discrete bending energy: the dot product is the cosine of the angle between the normals to adjacent cells and so, for small deflections, the parenthesis grows as one half of the square of this angle. This term tends to keep normals of adjacent cells aligned, much like spins in the classical Heisenberg model of ferromagnetism (20). This bending energy has been used in previous work to model elastic shells using triangulated surfaces, see for instance (21, 22), and it has been shown to be equivalent to the usual bending energy in the continuous limit (23). We will show in the following that a suitable choice of B allows one to adjust the vertex model rigidity to match that of the tissue under consideration.

2.2 Contractile contour

An additional contractile contour in the epithelium is implemented in the vertex model through the additional energy term,

$$\mathcal{E}_\Gamma = \Gamma \sum_{e \in C} L_e. \tag{4}$$

The geometry of the lattice is defined by two integers P_1 and P_2 with $0 < P_1 < P_2$, see figure 2A: the diameter of the contour C is $(2\,P_1 + 1)$ cells, and the diameter of the entire lattice is $(2\,P_2 + 1)$ cells. The number of cells inside the contractile contour C is $n_1 = 1 + 3\,P_1\,(P_1 + 1)$, and the total number of cells is $n_2 = 1 + 3\,P_2(P_2 + 1)$.

2.3 Numerical Code

With the aim to investigate the effect of the contractile contour, we have implemented a `C++` code to solve the vertex model numerically: the code solves the equilibrium using Newton-Raphson iterations, by cancelling the residual force vector on all vertices. This employs the Armijo line search (24) featuring quadratic convergence. The code relies on the `armadillo C++` linear algebra library (25). It is initialized with the reference configuration REF, such that cells have unit area, $A^0 = 1$. For $\Gamma = 0$ and with a free outer boundary, the sheet shrinks to a planar flat equilibrium configuration with uniform cell size (configuration PE). Next, the inhomogeneous contractile force Γ is increased in small steps, with vertices lying along the tissue boundary immobilized at the position found in configuration PE: this yields configurations F indexed by the value of Γ, which can be planar or non-planar.

2.4 Linear Stability

In addition, we investigated the stability of equilibria by computing their tangent stiffness matrix, which is the Hessian matrix of the energy with respect to vertex position or, equivalently, minus the jacobian matrix of the residual force. If the sign of the smallest (real) eigenvalue of this matrix is positive, the equilibrium is stable under energy-minimizing dynamics. If it is negative, the equilibrium is unstable. The jacobian is calculated using finite differences, and its smallest eigenvalue and the corresponding eigenvector are obtained via inverse power iterations (24). When Γ passes Γ_c, the planar equilibria become unstable: we compute buckled solutions by perturbing the planar solution along the leading eigenvector of the stability analysis.

2.5 Homogenization of a hexagonal lattice

We propose a derivation of a continuous plate model from the vertex model. It is based on a variant of the Cauchy-Born rule for hexagonal lattices, which we briefly review here.

The Cauchy-Born rule (26, 27) is applicable to the analysis of simple Bravais lattice. It considers homogeneous deformations $\mathbf{x}_v = \mathbf{F} \cdot \mathbf{X}_v$, where $\mathbf{X}_v$ is the reference position of the vertex v (or the atom v in a crystal), $\mathbf{x}_v$ is actual position, and $\mathbf{F}$ is an arbitrary deformation gradient. For a sheet embedded in the Cartesian 3D space, $\mathbf{F}$ is a 3×2 matrix. The homogenization is carried out by calculating the energy of the lattice in terms of the invariants of $\mathbf{F}$, and by identifying the result with an elastic energy. This captures the energy of configurations such that the deformation gradient varies on a length-scale much larger than the lattice parameter L^0.

We consider a hexagonal lattice, which is made up of *two* sublattices. For complex lattices like this one, the Cauchy-Born rule must be extended to allow for an independent translation of its sublattices, see for instance (26). For the hexagonal lattice, this reads $\mathbf{x}_v = \mathbf{F} \cdot \mathbf{X}_v \pm \frac{\mathbf{p}}{2}$, where $\mathbf{p}$ is a vector called the microscopic shift and the sign $\pm$ is alternating depending on which sublattice the vertex v belongs to, see figure S1 in Supplemental Information (S.I.). Note that the vertices are not in equilibrium except for a special value of $\mathbf{p}$, usually non-zero, depending on the macroscopic deformation gradient. The first and second gradients of the energy with respect to $\mathbf{p}$ define a stress and moduli, respectively, and this is known as 'inner elasticity' (26). In this context, $\mathbf{F}$ is a macroscopic deformation gradient and we call $\pm\frac{\mathbf{p}}{2}$ the microscopic displacement. The

homogenization is then carried out by expressing the energy in terms of $\mathbf{F}$ and $\mathbf{p}$, minimizing it with respect to $\mathbf{p}$ (*relaxation* step), and identifying the relaxed energy, now a function of $\mathbf{F}$, with that of an equivalent elastic continuum.

This procedure captures the dependence of the energy on the first gradient $\mathbf{F}$, but is unable to account for bending of the sheets which depend on curvature, *i.e.* on the second gradient of displacement. The Cauchy-Born rule must be extended one more time to capture the bending energy of a 2D lattice—this question has received considerable interest recently for the analysis of single-walled carbon nanotubes, see for instance (28–30). The two sublattice structure of the hexagonal lattice is also well-known to lie at the root of the peculiar band structure of graphene (31). Extensions of the Cauchy-Born rule have been proposed to deal with curvature, by means of the exponential map (32) or by pushing the expansion of the displacement to second order (29, 30).

We propose a simpler method, which is particularly suited to the analysis of small perturbations near a given configuration. In what follows, we first relax the residual stress in the lattice by means of a uniform stretching $a\,\mathbf{X}$, and analyze small perturbations near this configuration. All equations are systematically linearized with respect to the amplitude of the perturbation. In this linear context, one can treat the various Fourier modes separately. Therefore, we assume that the macroscopic position is $\mathbf{x}_v^{\text{macro}} = a\,\mathbf{X}_v + \Re(\hat{\mathbf{u}}\, e^{i\,\mathbf{k}\cdot\mathbf{X}_v})$, and that the microscopic displacement reads $\mathbf{u}_{\text{micro}} = \pm\Re(\frac{\hat{\mathbf{p}}}{2}\, e^{i\,\mathbf{k}\cdot\mathbf{X}_v})$. Here, $\Re$ denotes the real part, $\hat{\mathbf{u}}$ and $\hat{\mathbf{p}}$ are complex vectors capturing the macroscopic and microscopic perturbations, respectively, and $\mathbf{k}$ is the wavevector. Note that in the linear setting, only microscopic and macroscopic displacements corresponding to the same wavenumber $\mathbf{k}$ can be coupled. Summing the two contributions, we consider deformed configurations of the form

$$\mathbf{x}_v = a\,\mathbf{X}_v + \Re\left(\left(\hat{\mathbf{u}} \pm \frac{\hat{\mathbf{p}}}{2}\right) e^{i\,\mathbf{k}\cdot\mathbf{X}_v}\right). \tag{5}$$

Our homogenization method is carried out by considering the limit $|\mathbf{k}| \to 0$, combining with appropriate scaling assumptions on $\hat{\mathbf{u}}$ and $\hat{\mathbf{p}}$, and calculating an expansion of the energy in terms of $\hat{\mathbf{u}}$ and $\hat{\mathbf{p}}$. This is done in §S1 in the S.I., and summarized in §3.1 below.

3 Results

3.1 Continuous elastic plate approximation

The vertex model provides a quantitative description of the forces produced at the cell level in response to deformation. For weakly deformed cells, these forces increase linearly with the deformation. Thus, at the tissue level, one expects the epithelium to behave like an elastic sheet when the cells are weakly deformed (but the global deformation of the tissue can nonetheless be important). Our aim is to support this intuition by an explicit calculation and, importantly, to quantitatively relate the sheet elastic moduli to the cell level parameters G, H and B. We thus analyze below the energy changes associated with macroscopic deformations that vary on scales large compared to the cell size, such that the cells are weakly deformed. We proceed in two steps. We first determine the equilibrium planar configuration for the regular epithelium that we consider, building up on previous studies (3, 13) that investigated this question. We then examine the energy costs associated with non-planar deformations of this equilibrium configuration. A simple example of the long-wavelength approximation in a cell-modeling context is provided by ref. (33) where the approximation is used in one dimension.

We restrict ourselves to an epithelium consisting of identical, hexagonal cells ($n = 6$). Thus, the 'reference' vertex configuration is a regular hexagonal lattice with faces having unit area $A^0 = 1$. From planar geometry, the edge length of this reference lattice is $L^0 = \sqrt[4]{4/27}$. The line tension (term proportional to G in the energy) and the perimeter elasticity (proportional to H) both induce in-plane stress in the lattice. If the lattice is not held by boundary conditions, it relaxes this stress and assumes an equilibrium configuration of minimal energy. We seek this minimal energy configuration as a uniformly scaled hexagonal lattice, with

cells of area a^2 and edges of length $(a\,L^0)$. In this planar equilibrium configuration, the energy per cell reads

$$\epsilon_{\rm PE}(a) = \frac{1}{2}\left(1-a^2\right)^2 + \sqrt{2}\,\sqrt[4]{3}\,a\,G + 4\,\sqrt{3}\,a^2\,H. \tag{6}$$

When the energy $\epsilon_{\rm PE}(a)$ is minimum, a is a root of $\epsilon'_{\rm PE}(a)=0$. Depending on the values of the parameters G and H, this equation may have zero, one, or several positive roots a. The absence of a positive root signals the absence of an equilibrium configuration: the area elasticity term is too weak to counterbalance the line tension and the perimeter elasticity, and the lattice collapses (see (13) for details). When multiple roots exist, we consider the only one that corresponds to a minimum of $\mathcal{E}_{\rm vm}$. To avoid solving the cubic equation $\epsilon'_{\rm PE}(a)=0$ for a, we view a as a free parameter and G as a dependent variable, and solve the equation for G instead:

$$G(a) = a\,\frac{\sqrt{2}}{\sqrt[4]{3}}\,(1-a^2-4\,\sqrt{3}\,H). \tag{7}$$

Consider now a small perturbation from this *planar equilibrium* configuration 'PE', resulting in a *final* configuration 'F'. Because the hexagonal lattice is not a simple Bravais lattice, this perturbation is the sum of a smooth *macroscopic* displacement, and a rapidly oscillating *microscopic* displacement, see §2.5. We denote by $\mathbf{x}_v = a\,\mathbf{X}_v + v_X(\mathbf{X}_v)\,\mathbf{e}_X + v_Y(\mathbf{X}_v)\,\mathbf{e}_Y + w(\mathbf{X}_v)\,\mathbf{e}_Z$ the 'macroscopic' deformed position of a vertex, as obtained by averaging out the oscillatory microscopic displacement. The microscopic displacement is not represented here, but is correctly accounted for by our effective elastic moduli. Note that the displacement (v_X, v_Y, w) is sought as a function of the Lagrangian variable $\mathbf{X}_v$, the vertex position in reference configuration. As summarized below and detailed in §S1 of S.I., we find that the energy of the lattice in the final configuration F is described by an elastic plate model in the continuous limit, $\mathcal{E}_{\rm vm} \approx \mathcal{E}_{\rm plate}$ where

$$\mathcal{E}_{\rm plate} = \frac{1}{2}\iint \left(\lambda\,\mathrm{tr}^2\,\mathbf{E} + 2\,\mu\,|\mathbf{E}^2| + \beta\,(\Delta w)^2\right)\,\mathrm{d}X\,\mathrm{d}Y. \tag{8}$$

Here, $\mathbf{E}$ denotes the macroscopic Cauchy-Green tensor measuring stretching (34, 35), $|\mathbf{E}^2| = \mathrm{tr}(\mathbf{E}\cdot\mathbf{E})$ its invariant, and $w(X,Y) = \mathbf{x}\cdot\mathbf{e}_Z$ the lattice deflection along the Z-direction, *i.e.* away from the reference configuration lying in the (X,Y)-plane. The Laplacian operator in the bending term makes use of the reference coordinates, $\Delta = \partial^2/\partial X^2 + \partial^2/\partial Y^2$. The components of $\mathbf{E}$ read, for small deformations (the so-called Föppl-von Kármán approximation) (34, 35), $E_{ij} = 1/2(\partial_i v_j + \partial_j v_j) + (1/2\,a)\,\partial_i w\,\partial_j w$, where the last term couples planar and non-planar displacements and plays a crucial role in the analysis of buckling. Note that the simple form of Eq. (8) reflects our assumption of a small strain in the lattice plane.

To prove the equivalence $\mathcal{E}_{\rm vm} \approx \mathcal{E}_{\rm plate}$, we need only consider a single, representative cell: this is the central cell in the S.I. We consider a trial displacement of the form given in equation (5), obtained by the superposition of a uniform stretch with ratio a bringing the lattice to a stressfree configuration 'PE', a smooth (macrosopic) displacement captured by the complex amplitude vector $\hat{\mathbf{u}}$, and an oscillatory (microscopic) displacement captured by the complex shift vector $\hat{\mathbf{p}}$. Both the macroscopic and microscopic displacement are modulated harmonically with a 2D wavevector $\mathbf{k} = \eta\,\mathbf{K}$ where $\eta \to 0$ is an expansion parameter. We show in §S1 that the energy of the vertex model is asymptotically equivalent to that of the plate model in the long wavelength limit, $\eta \to 0$. To do so, we find the optimum microscopic displacement $\hat{\mathbf{p}}$ corresponding to a prescribed macroscopic displacement $\hat{\mathbf{u}}$, insert the result into the energy of the vertex model, and identify the relaxed energy with the continuous plate energy in equation (8).

The identification yields the following expressions for the stretching moduli λ and μ and for the bending modulus β, see §S1 of S.I.,

$$\lambda = -1 + 2\,a^2 + 2\,\sqrt{3}\,H \tag{9a}$$

$$\mu = \frac{1}{2}\,(1-a^2) \tag{9b}$$

$$\beta = \frac{\sqrt{3}}{a^2}\,B + \frac{1-a^2}{8\,\sqrt{3}}. \tag{9c}$$

These expressions for the Lamé coefficients λ and μ correct those derived by Staple (13) in the planar case, see S1.8 for details. With equations (9a-9c), we have completely specified the plate model towards which the vertex model converges in 3D. The conditions warranting that the plate energy is positive definite (material stability) are discussed in §S1.7 in the S.I: for instance, when $H = 0$, stability requires $0 < G < 0.4136$.

The limit where both G and H are small is worthy of attention, as a is then close to 1 by equation (7). This brings in two simplifications: (i) the mapping from the reference to the equilibrium configuration is infinitesimal and so there is no need to distinguish between these configurations; (ii) the expressions of the moduli can be linearized with respect to the small quantities G, H and $(1-a)$. This yields

$$G_{\rm lin} = \frac{2\sqrt{2}}{\sqrt[4]{3}}\left((1-a) - 2\sqrt{3}\,H\right) \tag{10a}$$

$$\lambda_{\rm lin} = 1 + \left(2\sqrt{3}\,H - 4\,(1-a)\right) \tag{10b}$$

$$\mu_{\rm lin} = 1-a \tag{10c}$$

$$\beta_{\rm lin} = \sqrt{3}\,B + \frac{1-a}{4\sqrt{3}}. \tag{10d}$$

In this limit, $\lambda_{\rm lin}$ converges to 1 but $\mu_{\rm lin}$ goes to zero: as a result, the plate model tends to preserve area (this is obvious from the discrete equation (1) since the area term becomes formally dominant over the other terms which provide shear and bending resistance). For 2D deformable bodies, Poisson's ratio reads $\nu = \lambda/(2\,\mu + \lambda) \approx 1 - 2\,(1-a)$ which is indeed close to the area-preserving limit $\nu = 1$ (2D 'incompressibility'). Another interesting fact is that the homogenized bending modulus $\beta_{\rm lin}$ has two contributions, see equation (10d): the first one, $\sqrt{3}\,B$, is independent of a but disappears if the discrete bending term is omitted in the model ($B = 0$); the second term, $(1-a)/(4\sqrt{3})$, which we call a *residual* bending modulus, is present even if $B = 0$. It is impossible to bend a hexagonal mesh while preserving all edge lengths and face areas: a hexagonal mesh is *geometrically rigid*. The energy of the vertex model must therefore increase when the configuration goes from planar to non-planar, even when no explicit bending energy is considered (*i.e.*, even for $B = 0$): this gives rise to the residual bending modulus. In real epithelia, the geometric rigidity of the mesh is likely irrelevant and there are many other mechanisms that lead to an effective bending rigidity, including 3D deformations of the cells, and the stiffness of the surrounding tissues. The role of the explicit coefficient B included in the extended vertex model is to effectively capture all these mechanisms.

To summarize, we have shown that the extended vertex model is equivalent to a thin plate in the long-wavelength limit, and have identified the elastic moduli of the equivalent plate. The case where the parameter a is close to 1 is particularly simple: then, the mesh almost preserves area and simpler expressions for the moduli have been derived. We have identified a small residual bending rigidity having a geometrical origin when $B = 0$, and have argued that the explicit bending term which we introduced in equation (1) allows for a more realistic and better controlled description of bending in real epithelia.

3.2 A test case: buckling driven by tissue inhomogeneity

Planar vertex models have successfully been used to capture experimental phenomenology, such as the influence of mechanically-driven cell rearrangements on epithelial cell patterns and morphogenesis (3, 4) as well as to infer epithelial tissue internal stresses (6, 36) and to examine their influence on cell proliferation (12). A recent study (17), which motivated the present work, has initiated the use of vertex models for the study of non-planar epithelium deformations. Specifically, appendage formation in *D. melanogaster* has been attributed to the three-dimensional deformations of the fly egg follicle epithelium caused by in-plane forces; simulations of a vertex model featuring an inhomogeneous distribution of line tension produced buckled shapes which compared well to real epithelia.

In this section, we use a variant of the geometry from (17) to test both our vertex model and our continuous plate model. We show that the simulation results are very sensitive to the value of the bending modulus B, which has been ignored in previous work. We also show that the continuous plate model can be used to rationalize the following phenomenon: the continuous model features buckled solutions similar

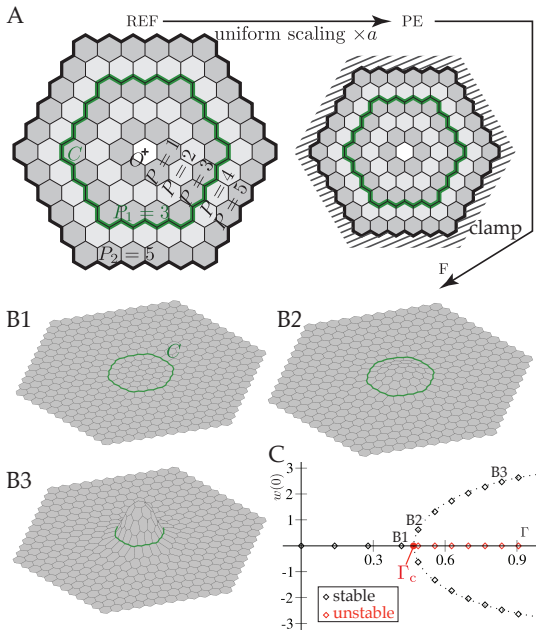


Figure 2: **Buckling in the vertex model driven by a contractile contour** C. Panel A: starting from the reference configuration 'REF', here with geometrical parameters $(P_1, P_2) = (3, 5)$, a uniform scaling a is applied until a planar equilibrium 'PE' is reached; then, the outer boundary is clamped, and we track 3D equilibrium solutions 'F'. Panels B1–B3: three equilibrium configurations with $(G, H, B) = (0.254, 0, 0.0534)$ and $(P_1, P_2) = (3, 11)$: (B1) below threshold, $\Gamma = 0.418$; (B2) just above the threshold, $\Gamma = 0.488$; (B3) well above threshold, $\Gamma = 0.836$. Panel C: bifurcation diagram displaying buckling threshold $\Gamma_c = 0.468$. Dotted curve is a guide to the eye.

to those of the discrete model in the presence of an inhomogeneous line tension, and yields an accurate prediction for the buckling threshold as a function of all the parameters of the problem.

3.2.1 Numerical investigation

A simplified version of the geometry considered in (17) is sketched in figure 2A. A contractile contour C is embedded inside a lattice. It represents the 'actin cable' observed in the experiments, that displays a high concentration of the motor protein myosin (17). In our model, the edges belonging to the contour are assigned a line tension $(G+\Gamma)$ which is larger than the line tension G of the other edges, see §2.2 for details.

We carry out a numerical and analytical buckling study based on the total energy $\mathcal{E}_{\rm vm} + \mathcal{E}_\Gamma$, when the inhomogeneity of the line tension Γ is progressively (and uniformly) increased.

Given the values of the parameters (G, H, B) of the extended vertex model, we first let the lattice relax to its planar equilibrium configuration 'PE', by applying a uniform scaling a such that $\epsilon'_{\rm PE}(a) = 0$. Next, we clamp the outer boundaries by restraining the motion of the outer vertices in all directions. Finally, we increase Γ progressively and track the equilibrium shapes of the inhomogeneous lattice numerically using Newton–Raphson iterations. Their stability is examined using standard eigenvalue analysis (see Materials and Methods for details). When the inhomogeneity Γ is smaller than some threshold $\Gamma_{\rm c}$, the equilibrium solution remains planar, albeit non-homogeneous: the contractile contour tends to become circular, and the region inside the contour is compressed, see figure 2B1. Beyond the threshold value $\Gamma_{\rm c}$, this planar solution becomes unstable, and a pair of stable non-planar solutions appears (figure 2B2–C). These buckled solutions are mirror-symmetric to each other, with respect to the clamping plane $z = 0$. When plotted as a function of the control parameter Γ, the maximum deflection $w(0)$ traces out a bifurcation diagram which is typical

of a supercritical pitchfork bifurcation, see figure 2C, and is similar to that of the well-studied Elastica, see e.g. (34, 35). In particular, the maximum tissue deflection grows like $\sqrt{\Gamma - \Gamma_c}$ close to threshold.

3.2.2 Buckling in the plate model

The reported simulations show that inhomogeneous tissue properties can lead to buckling, and that the extended vertex model captures this phenomenon. We now show that a detailed account of this buckling phenomenon is possible based on the continuous plate model obtained earlier via homogenization. To this end, we introduce a variant of the buckling problem in a continuous, axisymmetric geometry, see Figure 3A.

We consider the limit $G, H, \Gamma \ll 1$ and $a \approx 1$ where the homogenized plate model almost preserves areas, and strains remain small. Using these assumptions, the buckling analysis can be carried out analytically using the Föppl-von Kármán equations for plates. The extension of the buckling analysis to finite values of G, H, Γ is straightforward but requires numerical integration. The problem is similar to the budding of a domain in a membrane driven by line tension at the domain edge which was treated using approximate energy considerations in (37, 38). The highly strained limit where sharp localized folds appear would also be interesting to study. However, this would require entirely different techniques and it lies beyond the scope of the present work.

We define the inner and outer radii R_1 and R_2 for our continuous problem by matching the areas in the reference configurations: πR_1^2 is matched with the number of cells inside the contour, n_1, and πR_2^2 with the total number of cells, n_2: $R_1 = f(P_1)$ and $R_2 = f(P_2)$ where $f(P) = \sqrt{(1 + 3P(P+1))/\pi}$ and P_1 and P_2 are integers measuring the radius of the contractile contour and of the outer tissue boundary, see figure 2A and §2.2. Note that $f(P) \approx P + 1/2$ to within 3% for any value of P. As a result, R_1 and R_2 are close to the average radii of the contour C and of the external boundary, respectively.

In axisymmetric geometry, the displacement and strain are functions of the radial coordinate $R = \sqrt{X^2 + Y^2}$, and independent of the polar angle Θ. We denote by $(\mathbf{e}_R(\Theta), \mathbf{e}_\Theta(\Theta))$ the local polar basis, and seek the displacement in the axisymmetric form $\mathbf{u}(R, \Theta) = v(R)\,\mathbf{e}_R(\Theta) + w(R)\,\mathbf{e}_Z$ for $0 < R < R_2$. By symmetry, the Cauchy-Green strain writes $\mathbf{E} = E_R\,\mathbf{e}_R \otimes \mathbf{e}_R + E_\Theta\,\mathbf{e}_\Theta \otimes \mathbf{e}_\Theta$, where the Föppl-von Kármán expression of the principal strain is used, $E_R = v'(R) + w'^2(R)/2$ and $E_\Theta = v(R)/R$.

We introduce a continuous approximation of the discrete energy of the contractile circle,

$$\mathcal{E}_\Gamma = 2\,\pi\,\Gamma\,R_1\,(1 + E_\Theta(R_1)). \tag{11}$$

As in the discrete setting, see Eq. (4), the perimeter of the deformed contractile circle, $R_1(1 + E_\Theta)$, is multiplied by the line tension Γ. We solve the circular plate buckling problem by minimizing the total energy $\mathcal{E}_{\text{plate}} + \mathcal{E}_\Gamma$, using the linearized expressions of the moduli in Eq. (10).

We start by considering a planar solution, $w(R) = 0$, which we use as the base solution for our buckling analysis. The complete solution of this planar, axisymmetric problem of linear elasticity is worked out in §S2. The stress obtained in this way is called the *pre-stress*. Its principal values are denoted by $S_R(R)$ and $S_\Theta(R)$. In the limit of 2D 'incompressibility' which we consider here ($a \approx 1$), the solution is particularly simple:

$$\begin{aligned} S_R(R) = S_\Theta(R) &= -S^*\,t(R) \\ \text{where } t(R) &= \begin{cases} 1 & \text{if } R < R_1 \\ -\frac{1}{\alpha^2 - 1} & \text{if } R_1 < R. \end{cases} \end{aligned} \tag{12}$$

Here, $\alpha = R_2/R_1$ is a geometrical parameter, and $S^* = ((\alpha^2 - 1)/\alpha^2)\,(\Gamma/R_1)$ is a typical membrane stress. In the limit considered, the pre-stress is locally isotropic, piecewise constant, and independent of the elastic moduli. It is compressive in the interior region $R < R_1$ (where $S_R = S_\Theta < 0$), which drives the buckling instability, and tensile in the outer region ($S_R = S_\Theta > 0$).

We can now proceed to investigate the axisymmetric buckling of the plate using linear stability analysis. In axisymmetric geometry, the equation for the transverse equilibrium of the plate obtained by variation of

the energy in Eq. (8) reads, when linearized near the pre-stressed configuration, see for instance (39, 40):

$$\beta_{\rm lin}\left(-\frac{1}{R}\frac{\mathrm{d}(R\,q')}{\mathrm{d}R}+\frac{q}{R^2}\right)-S^*\,t(R)\,q(R)=0. \tag{13}$$

Here, $q(R)=w'(R)$ is the radial slope. The boundary conditions are the continuity condition $q(0)=0$, and the clamping condition $q(R_2)=0$ (the clamping condition on the outer edge arises when going from the hexagonal to the perfectly axisymmetric geometry, see §S3). When solutions $q(R)$ exist, this indicates that the buckling load has been reached. This stability problem depends solely on the dimensionless geometric parameter $\alpha=R_2/R_1$ and on the dimensionless tension $\gamma=S^*\,R_1^2/\beta=(\Gamma\,R_1/\beta)\,((\alpha^2-1)/\alpha^2)$. We conclude that buckling occurs when γ reaches a critical value that is a function of the aspect-ratio α only, $\gamma=\gamma_{\rm c}(\alpha)$. The function $\gamma_{\rm c}(\alpha)$ can be found by solving Eq. (13) in terms of Bessel functions in the inner ($R<R_1$) and outer ($R>R_1$) regions, and matching them across the contractile circle $R=R_1$, see §S3. The dimensionless buckling threshold varies in the range $\gamma_{\rm c}(\alpha=\infty)=5.78$ when clamping is applied at infinity ($R_2\gg R_1$), to $\gamma_{\rm c}(\alpha=1)=14.68$ when clamping is applied immediately outside the contracting circle ($R_2=R_1$) as in the analysis of circular de-lamination blisters (40). Our analysis also provides the exact solution for the budding of a membrane domain driven by line tension considered in (38) (the approximate analysis of (38) considered a spherical cap budding from a plane and ignored the bending energy in the circular ridge; it predicted a dimensionless buckling threshold equal to 8 and a subcritical transition, in contrast to what we find here).

Finally, we compare results of our buckling analysis for the plate model to the numerical results obtained with the extended vertex model, limiting ourselves to the case $H=0$ for simplicity. Expressing $\beta_{\rm lin}$ in terms of the parameters of the vertex model by Eqs. (10d) and (10a), we predict a buckling threshold $\Gamma=\Gamma_{\rm c}$, for $H=0$:

$$\Gamma_{\rm c}=\gamma_{\rm c}(\alpha)\,\frac{\alpha^2}{\alpha^2-1}\,\frac{1}{R_1}\,\left(\frac{G}{8\sqrt{2}\,\sqrt[4]{3}}+\sqrt{3}\,B\right). \tag{14}$$

Figure 3B displays the buckling threshold vs. tissue size $R_2=\alpha\,R_1$ as predicted by this equation, together with our numerical results for the vertex model. Despite the simplification of a radially symmetric, continuous geometry, the plate model closely agrees with the discrete simulation results. The buckling threshold decreases with the tissue size R_2 and quickly reaches an asymptote $\Gamma_c=\Gamma_c^\infty$. This decrease is because the clamp on the outer boundary hinders the buckling, but this finite size effect quickly fades out as $\alpha=R_2/R_1$ becomes larger than ≈ 2. We observed similar agreement between the analytical results and the vertex model simulations when other geometric or material parameters were varied. In particular, Fig. S3 demonstrates the existence of a residual modulus in the vertex model for $B=0$ (thus a non-zero buckling threshold Γ_c), and shows that the dependence of the buckling threshold Γ_c on the bending modulus B predicted by Eq. (14) is accurate. The mode shape is predicted with excellent accuracy by the continuous plate model as well, see Figure 3C. Note that we have compared the buckling threshold and the rescaled mode shapes, but not the buckling amplitudes: to predict the buckling amplitude based on the plate model (for comparison with the data shown in figure 2C), a weakly nonlinear analysis or a nonlinear simulation of the plate model are required. This goes beyond the linear analysis presented here. Observe that the solution shown in 2B3 displays large strain and large curvature: the assumptions of our linearly elastic plate model are not justified in this deeply post-buckled regime.

Finally, we note that an experimental test of relation (14) would require quantitative measuring of the cable tension and bending rigidity. Inhomogeneities in line tension can be assessed by recoil after laser-cutting experiments (1). Line tension can also be quantitatively measured by dynamic tissue perturbations with optical tweezer, a recently developed technique (41). This technique also appears very appropriate for direct measurement of the bending rigidity.

4 Discussion and conclusion

In this work, we have proposed an extended vertex model for studying non-planar epithelial deformations, including explicitly a discrete bending energy. We have shown that this model reduces to the usual elastic

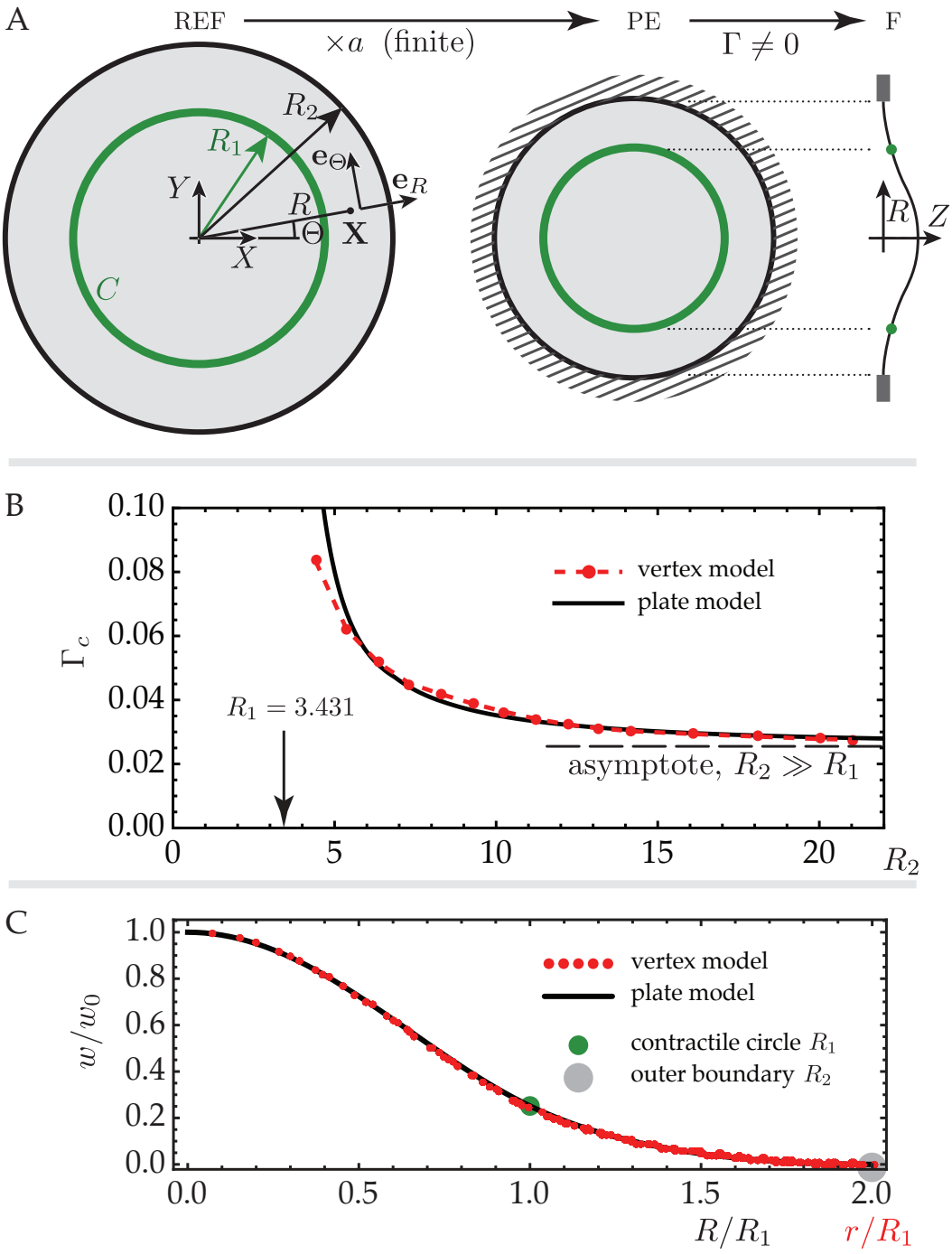


Figure 3: **Buckling in the continuous setting, and comparison to results of the vertex model for** $(G, H, B) = (0.0351, 0, 0.00738)$**.** A: equivalent continuous, axisymmetric geometry; buckling of a circular plate having a clamped outer edge, subjected to contraction along an embedded circle (green). The buckled configuration F is represented after cutting through the plane (ORZ) containing the axis of symmetry. B: buckling threshold as a function of the outer radius R_2 with fixed inner radius $R_1 = 3.431$. C: comparison of the shapes $w(R)$ of the buckling modes rescaled by the deflection w_0 at the center, with $(P_1, P_2) = (8, 16)$ in the vertex model and $\alpha = R_2/R_1 = 2$ in the plate model, immediately above the buckling threshold $\Gamma = 0.0217 > \Gamma_c = 0.0194$. For the vertex model, each datapoint corresponds to a simulation vertex, with r being its distance to axis (Oz) and w its deflection, both measured in buckled configuration. Since G is small and $H = 0$, we use the linearized moduli in the plate model for panels B and C.

plate description in the limit of a long wavelength compared to the scale of a single cell. We used a systematic method for deriving the plate model, which can be extended to other types of mesh and energy function.

For simple lattices, the traditional Cauchy-Born approximation assumes that the vertex displacements are given by a linear mapping. The hexagonal network being a complex lattice in the sense of Bravais, the Cauchy-Born approximation has been extended by introducing a shift $\mathbf{p}$ capturing the relative translation of the two sublattices: the associated microscopic displacement has alternating signs from one vertex to its neighbors. In the context of Fourier analysis, we have calculated the complex shift $\hat{\mathbf{p}}$ in terms of the complex amplitude $\hat{\mathbf{u}}$ of the macroscopic (averaged) displacement: as a result, our homogenized plate moduli correctly take into account the microscopic oscillatory displacement, even though there is no need to account for it in the continuous plate model. A clear—although unintentional—demonstration of the existence of this microscopic displacement is given in reference (42), where the authors impose an affine displacement to all vertices lying on the boundary of a 2D rectangular patch. These conditions are incompatible with the existence of an oscillatory microscopic displacement; effectively, they impose $\mathbf{p} = \mathbf{0}$ along the boundary. As a result, they obtain a non-affine solution, which we can describe as follows in light of our analysis: the solution described by the generalized Cauchy-Born rule (homogeneous solution plus oscillatory displacement, $\mathbf{p} \neq \mathbf{0}$) is reached deep in the interior of the domain and a boundary layer builds up to connect the interior with the domain boundary, where $\mathbf{p} = \mathbf{0}$. This boundary layer is a few cells thick, and could be described quantitatively by accounting for the strain energy associated with the gradient of $\mathbf{p}$, see for instance (29).

We have also applied the discrete vertex model and the continuum plate model to 3D epithelial deformations by investigating the buckling of an epithelial sheet induced by a contracting circle. In both descriptions, we have found a supercritical bifurcation at a well-defined threshold, and the plate model enabled us to capture the dependence of the buckling threshold on the model parameters. Our analysis of buckling made use of several approximations, like that of an axisymmetric geometry and of small deformations while the numerics was performed in an hexagonal geometry which produced some regions of high strain. Moreover, we neglected in our energetic analysis the localized relaxation of the microscopic displacement between the two sublattices of the hexagonal lattice. In spite of these simplifying assumptions, the plate model was found to account quite accurately for the numerical results of the vertex model. Therefore, we expect similar analyses to prove useful for analyzing buckling in different contexts, as in the case of budding membrane domains (38). Our results for a contractile circle show that the buckling threshold quickly asymptotes to a limiting value as the size of the outer ring is increased. Buckling in a given region is thus localized and independent of morphogenetic events taking place elsewhere in the tissue. As a result, a large tissue could be morphed into a complex shape by the superposition of multiple buckling events in different regions. The simplest instance of this mechanism was previously found in (17) for the formation of dorsal appendage primordia in the Drosophila egg. We anticipate that other examples will be found, perhaps with the added complications of cell proliferation and deformation within the patch (43).

There are different interesting avenues for future development. One will consist in linking the phenomenological parameters of our cell model to those of more detailed, three-dimensional cell-based descriptions, that, for instance, capture cell volume explicitly as in (44) or (45). This would allow one to investigate how tissue rigidity arises and is regulated at the cell level. We also expect the proposed model and the demonstated link to continuum mechanics to be useful for the analysis of diverse biological problems where morphogenesis relies on cell mechanics (46). In this respect, it should be noted that the proposed vertex model can easily be modified to include spontaneous curvature (by introducing a non-zero rest angle between normals of neighboring cells). In this case, we expect buckling to appear via an imperfect pitchfork bifurcation. This is relevant for a whole family of biological problems where cells make use of differential apico-basal contractions, like gastrulation (7). Finally, our results and methodology may prove interesting beyond biology in studying the folding and self-assembly of complex human-made elastic materials like origami metamaterials (47, 48).

Author contributions

Designed research: BA, NM, SYS, VH; performed research: BA, NM; contributed analytic tools: BA, IGK, NM; wrote the paper: BA, NM, SYS, VH.

Acknowledgments

NM, SYS, and BA acknowledge support from GrantRGP0052/2009 from the Human Frontiers Science Program. SYS also acknowledges support from the 1R01GM107103 grant from NIGMS. We are very grateful to the anonymous Referee who pointed to us the need to account for the microscopic displacement in the derivation of the continuous model.

References

1. Lecuit, T., P. F. Lenne, and E. Munro, 2011. Force generation, transmission, and integration during cell and tissue morphogenesis. *Annu. Rev. Cell Dev. Biol.* 27:157–184.

2. Martin, A. C., M. Gelbart, R. Fernandez-Gonzalez, M. Kaschube, and E. F. Wieschaus, 2010. Integration of contractile forces during tissue invagination. *J. Cell Biol.* 188:735–749.

3. Farhadifar, R., J.-C. Röper, B. Aigouy, S. Eaton, and F. Jülicher, 2007. The Influence of Cell Mechanics, Cell-Cell Interactions, and Proliferation on Epithelial Packing. *Current Biology* 17:2095–2104.

4. Rauzi, M., P. Verant, T. Lecuit, and P. F. Lenne, 2008. Nature and anisotropy of cortical forces orienting Drosophila tissue morphogenesis. *Nat. Cell Biol.* 10:1401–1410.

5. Bosveld, F., I. Bonnet, B. Guirao, S. Tlili, Z. Wang, A. Petitalot, R. Marchand, P. L. Bardet, P. Marcq, F. Graner, and Y. Bellaiche, 2012. Mechanical control of morphogenesis by Fat/Dachsous/Four-jointed planar cell polarity pathway. *Science* 336:724–727.

6. Sugimura, K., and S. Ishihara, 2013. The mechanical anisotropy in a tissue promotes ordering in hexagonal cell packing. *Development* 140:4091–4101.

7. Khan, Z., Y. C. Wang, E. F. Wieschaus, and M. Kaschube, 2014. Quantitative 4D analyses of epithelial folding during Drosophila gastrulation. *Development* 141:2895–2900.

8. Honda, H., 1978. Description of Cellular Patterns by Dirichlet Domains: The Two-Dimensional Case. *J. theor. Biol.* 72:523–543.

9. Honda, H., 1983. Geometrical models for cells in tissues. *Int. Rev. Cytol.* 81:191–248.

10. Sulsky, D., S. Childress, and J. Percus, 1984. A Model of Cell Sorting. *J. theor. Biol.* 106:275–301.

11. Graner, F., 1993. Can Surface Adhesion Drive Cell Rearrangement? Part II: A Geometrical Model. *J. theor. Biol.* 164:477–506.

12. Hufnagel, L., A. A. Teleman, H. Rouault, S. M. Cohen, and B. I. Shraiman, 2007. On the mechanism of wing size determination in fly development. *Proc. Natl. Acad. Sci. U.S.A.* 104:3835–3840.

13. Staple, D., R. Farhadifar, J.-C. Röper, B. Aigouy, S. Eaton, and F. Jülicher, 2010. Mechanics and remodelling of cell packings in epithelia. *Euro. Phys. J. E* 33(2):117–127.

14. Fletcher, A. G., M. Osterfield, R. E. Baker, and S. Y. Shvartsman, 2014. Vertex models of epithelial morphogenesis. *Biophys. J.* 106:2291–2304.

15. Mehes, E., and T. Vicsek, 2014. Collective motion of cells: from experiments to models. *Integr Biol (Camb)* 6:831–854.

16. Bardet, P. L., B. Guirao, C. Paoletti, F. Serman, V. Leopold, F. Bosveld, Y. Goya, V. Mirouse, F. Graner, and Y. Bellaiche, 2013. PTEN controls junction lengthening and stability during cell rearrangement in epithelial tissue. *Dev. Cell* 25:534–546.

17. Osterfield, M., X. Du, T. Schupbach, E. Wieschaus, and S. Shvartsman, 2013. Three-Dimensional Epithelial Morphogenesis in the Development of *Drosophila* Egg. *Developmental Cell* 24:400–410.

18. Weaire, D., and N. Rivier, 1984. Soap, cells and statistics-random patterns in two dimensions. *Contemporary Physics* 25:59–99.

19. Alexa, M., and M. Wardetzky, 2011. Discrete Laplacians on General Polygonal Meshes. *Transaction on Graphics (SIGGRAPH 2011)* 30:102.

20. De Gennes, P., and C. Taupin, 1982. Microemulsions and the flexibility of oil/water interfaces. *The Journal of Physical Chemistry* 86:2294–2304.

21. Kantor, Y., and D. R. Nelson, 1987. Crumpling transition in polymerized membranes. *Phys. Rev. Lett.* 58:2774–2777.

22. Kantor, Y., and D. R. Nelson, 1987. Phase transitions in flexible polymeric surfaces. *Phys. Rev. A* 36:4020–4032.

23. Grinspun, E., Y. Gingold, J. Reisman, and D. Zorin, 2006. Computing discrete shape operators on general meshes. *Eurographics (Computer Graphics Forum)* 25:547–556.

24. Burden, R., and J. Faires, 2011. Numerical Analysis. Cengage Learning, 9$^{\text{nd}}$ edition.

25. Sanderson, C., 2010. Armadillo: An Open Source C++ Linear Algebra Library for Fast Prototyping and Computationally Intensive Experiments. Technical Report Technical Report, NICTA.

26. Cousins, C. S. G., 1978. Inner elasticity. *Journal of Physics C: Solid State Physics* 11:4867–4879.

27. Ericksen, J. L., 1984. The Cauchy and Born Hypotheses for crystals. *In* M. E. Gurtin, editor, Phase Transformations and Material Instabilities in Solids. Academic Press, New York, 61–77.

28. Arroyo, M., and T. Belytschko, 2004. Finite crystal elasticity of carbon nanotubes based on the exponential Cauchy-Born rule. *Physical Review B (Condensed Matter and Materials Physics)* 69:115415.

29. Guo, X., J. B. Wang, and H. W. Zhang, 2006. Mechanical properties of single-walled carbon nanotubes based on higher order Cauchy-Born rule. *International Journal of Solids and Structures* 43:1276–1290.

30. Wu, J., K. C. Hwang, and Y. Huang, 2008. An atomistic-based finite-deformation shell theory for single-wall carbon nanotubes. *Journal of the Mechanics and Physics of Solids* 56:279–292.

31. Neto, A. C., F. Guinea, N. Peres, K. S. Novoselov, and A. K. Geim, 2009. The electronic properties of graphene. *Reviews of modern physics* 81:109.

32. Arroyo, M., and T. Belytschko, 2002. An atomistic-based finite deformation membrane for single-layer crystalline films. *Journal of the Mechanics and Physics of Solids* 50:1941—1977.

33. Fozard, J. A., H. M. Byrne, O. E. Jensen, and J. R. King, 2010. Continuum approximations of individual-based models for epithelial monolayers. *Math Med Biol* 27:39–74.

34. Landau, L. D., and E. M. Lifshitz, 1981. Theory of Elasticity (Course of Theoretical Physics). Pergamon Press, 2$^{\text{nd}}$ edition.

35. Audoly, B., and Y. Pomeau, 2010. Elasticity and Geometry: From Hair Curls to the Non-linear Response of Shells. Oxford University Press, Oxford, UK.

36. Chiou, K., L. Hufnagel, and B. Shraiman, 2012. Mechanical Stress Inference for Two Dimensional Cell Arrays. *PLoS Comput Biol* 8:e1002512.

37. Helfrich, W., 1974. The size of bilayer vesicles generated by sonication. *Physics Letters A* 50:115–116.

38. Lipowsky, R., 1992. Budding of membranes induced by intramembrane domains. *Journal de Physique II* 2:1825–1840.

39. Timoshenko, S., and J. Gere, 1961. Theory of elastic stability. MacGraw Hill, New York, 2nd edition.

40. Hutchinson, J., and Z. Suo, 1992. Mixed mode cracking in layered materials. *Adv. Appl. Mech.* 29:63–191.

41. Bambardekar, K., R. Clément, O. Blanc, C. Chardès, and P.-F. Lenne, 2015. Direct laser manipulation reveals the mechanics of cell contacts in vivo. *Proceedings of the National Academy of Sciences* 112:1416–1421.

42. Davit, Y., J. M. Osborne, H. M. Byrne, D. Gavaghan, and J. Pitt-Francis, 2013. Validity of the Cauchy-Born rule applied to discrete cellular-scale models of biological tissues. *Physical Review E* 87.

43. Chauhan, B. K., M. Lou, Y. Zheng, and R. A. Lang, 2011. Balanced Rac1 and RhoA activities regulate cell shape and drive invagination morphogenesis in epithelia. *Proc. Natl. Acad. Sci. U.S.A.* 108:18289–18294.

44. Honda, H., M. Tanemura, and T. Nagai, 2004. A three-dimensional vertex dynamics cell model of space-filling polyhedra simulating cell behavior in a cell aggregate. *J. theor. Biol.* 226:439–453.

45. Hannezo, E., J. Prost, and J.-F. Joanny, 2011. Instabilities of Monolayered Epithelia: Shape and Structure of Villi and Crypts. *Phys. Rev. Lett.* 107:078104–1–5.

46. Liang, H., and L. Mahadevan, 2011. Growth, geometry and mechanics of a blooming lily. *PNAS* 108:5516–5521.

47. Rammerstorfer, F., D. Pahr, T. Daxner, and W. Vonach, 2006. Buckling in Thin Walled Micro and Meso Structures of Lightweight Materials and Material Compounds. *Comput. Mech.* 37:470–478.

48. Ryu, J., M. D'Amato, X. Cui, K. Long, H. Qi, and M. Dunn, 2012. Photo-origami – Bending and folding polymers with light. *Appl. Phys. Lett.* 100:161908.